



Published in final edited form as:

Environ Sci Technol. 2013 July 2; 47(13): 6925–6934. doi:10.1021/es3045899.

Attachment of Pathogenic Prion Protein to Model Oxide Surfaces

Kurt H. Jacobson¹, Thomas R. Kuech², and Joel A. Pedersen^{1,2,3,*}

¹Department of Civil and Environmental Engineering, University of Wisconsin, Madison, WI 53706

²Environmental Chemistry and Technology Program, University of Wisconsin, Madison, WI 53706

³Department of Soil Science, University of Wisconsin, Madison, WI 53706

Abstract

Prions are the infectious agents in the class of fatal neurodegenerative diseases known as transmissible spongiform encephalopathies, which affect humans, deer, sheep, and cattle. Prion diseases of deer and sheep can be transmitted via environmental routes, and soil has been implicated in the transmission of these diseases. Interaction with soil particles is expected to govern the transport, bioavailability and persistence of prions in soil environments. A mechanistic understanding of prion interaction with soil components is critical for understanding the behavior of these proteins in the environment. Here, we report results of a study to investigate the interactions of prions with model oxide surfaces (Al_2O_3 , SiO_2) using quartz crystal microbalance with dissipation monitoring and optical waveguide light mode spectroscopy. The efficiency of prion attachment to Al_2O_3 and SiO_2 depended strongly on pH and ionic strength in a manner consistent with electrostatic forces dominating interaction with these oxides. The N-terminal portion of the protein appeared to facilitate attachment to Al_2O_3 under globally electrostatically repulsive conditions. We evaluated the utility of recombinant prion protein as a surrogate for prions in attachment experiments and found that its behavior differed markedly from that of the infectious agent. Our findings suggest that prions preferentially associate with positively charged mineral surfaces in soils (e.g., iron and aluminum oxides).

INTRODUCTION

Soil has been implicated in the indirect (environmentally mediated) transmission of chronic wasting disease (CWD) of North American members of the deer family and scrapie in sheep and goats.^{1–3} Scrapie and CWD are members of a class of inevitably fatal neurodegenerative diseases caused by prions and known as transmissible spongiform encephalopathies (TSEs). Other natural TSEs include bovine spongiform encephalopathy in cattle, Creutzfeldt-Jakob disease in humans, and transmissible mink encephalopathy (TME) in mink. Prions are infectious particles composed chiefly, if not entirely, of an improperly folded form of a cell

*Corresponding author address: Department of Soil Science, University of Wisconsin, 1525 Observatory Drive, Madison, WI 53706 1299; phone: (608) 263-4971; fax: (608) 265-2595; joelpedersen@wisc.edu.

Supporting Information

Text, tables, and figures. This material is available free of charge via the Internet at <http://pubs.acs.org>.

surface sialoglycoprotein denoted PrP.⁴ The properly folded form, referred to as cellular PrP or PrP^C, is expressed at high levels in central nervous system and lymphatic tissue.⁵ The disease-associated form (PrP^{TSE})⁶ is identical to PrP^C in amino acid sequence and covalent post-translational modifications. The only known differences between PrP^C and PrP^{TSE} are in folding: PrP^C has high (47%) α -helical and low (3%) β -sheet content while PrP^{TSE} is enriched in β -sheet content (43–54%) and contains little α -helical content.^{7,8} NMR structures of recombinant PrP (recPrP) from numerous species have been solved^{9–12} and are the best estimates of PrP^C structure.¹³ The insolubility of PrP^{TSE} and the disorder in its aggregates have prevented determination of its structure by solution-state NMR or x-ray crystallography.¹³ Electron crystallography, Fourier transform infrared spectroscopy, circular dichroism, x-ray fibril diffraction, and molecular modeling have provided insight into the structure of PrP^{TSE}, but none of the structural models proposed to date are entirely consistent with available biophysical data.^{8,14,15} The divergent conformations of PrP^{TSE} and PrP^C lead to marked differences in biophysical properties: PrP^C is monomeric, soluble in water and nondenaturing detergents, and sensitive to digestion by proteinase K (PK) while PrP^{TSE} forms ordered aggregates, is insoluble, and exhibits partial protease resistance. The central molecular event in prion disease propagation is the conversion of host-encoded PrP^C to PrP^{TSE}.

Prions enter soil environments through shedding in feces,^{16,17} urine,¹⁸ and saliva¹⁹ from infected animals, and decomposition of diseased carcasses.¹ Prions can also enter the environment as a result of disposal of infected material. Controlled pen experiments demonstrated that decomposed carcasses or residual excreta and secretions from CWD-infected animals were sufficient to transmit disease to naïve mule deer.¹ Prions can persist in soil for years,^{20,21} and ruminants consume soil both intentionally to supplement mineral nutrition and incidentally during feeding and grooming.^{22–24} Ingestion of prions associated with soil particles has been shown to enhance disease transmission, in some cases dramatically.^{25,26}

Assessing the risks posed by prions in soils requires understanding of the interaction of these proteins with mineral and organic soil particle surfaces. Previous studies investigated the attachment of prions to whole soils, soil minerals, and wastewater biosolids.^{27–34} While these studies allowed some inferences to be made about the strength of attachment (e.g., based on ease of extraction), current knowledge about the mechanisms governing prion interaction with most soil particle surfaces is limited. Furthermore, the above studies relied on solution depletion experiments and extraction of PrP^{TSE} from adsorbent surfaces (which is typically incomplete) or immunological detection of sorbed PrP^{TSE} (which is impacted by antibody epitope accessibility and appears to change over time in some systems³⁵). Advancing a mechanistic understanding of prion attachment to environmental surfaces requires experiments conducted with purified PrP, well-controlled solution conditions, well-defined surfaces, and direct quantification of the adsorbed protein.

The objective of this study was to evaluate the importance of electrostatic interactions on the attachment of infectious prion particles to charged, hydrophilic mineral surfaces. To achieve this objective, we investigated PrP^{TSE} attachment to and detachment from Al₂O₃ and SiO₂ surfaces using two real-time, label-free, *in situ* techniques: quartz crystal microbalance with

dissipation monitoring (QCM-D) and optical waveguide lightmode spectroscopy (OWLS). Our aim was to understand the interaction of the pathogenic PrP with these surfaces; we therefore employed *bona fide* PrP^{TSE} particles purified from brain tissue of experimentally infected animals. We used both nominally full-length pathogenic PrP (denoted below as PrP^{TSE}) and an N-terminally truncated form of the protein (PrP^{27–30}). The latter was used to examine the importance of the N-terminus on attachment and because pathogenic PrP released from decomposing carcasses may be in an N-terminally truncated state.³⁵ The techniques employed provide accurate *in situ* mass attachment data with high temporal resolution, and complementary use of these techniques allows determination of the amount of water incorporated in prion adlayers.

MATERIALS AND METHODS

Sources of PrP

Syrian hamsters (cared for according to all institutional protocols) were intracerebrally inoculated with the HY strain of hamster-adapted TME agent.³⁶ Upon manifestation of clinical symptoms animals were euthanized, brain tissue was harvested, and PrP^{TSE} was purified from the tissue using the procedure of Raymond and Chabry³⁷ modified to include two final rinses with buffer (3 mM HEPES (pH 7.0) with ionic strength (*I*) adjusted to 5 mM with NaCl) to minimize residual detergent in preparations, and resuspension in the same buffer. We treated preparations with proteases to degrade proteins co-purifying with PrP^{TSE}. We used thermolysin (Sigma-Aldrich, St. Louis, MO) to purify nominally full-length PrP^{TSE} (the N-terminus of PrP^{TSE} lacks thermolysin cleavage sites³⁸); PrP^{27–30} was prepared using PK (Promega, Madison, WI). Each hamster brain yielded 27–54 µg pathogenic PrP (see the Supporting Information (SI) for details). The purity of both preparations was assessed by SDS-PAGE with silver staining (Figure S1b; Pierce Silver Stain Kit, Rockford, IL), and densitometry revealed that PrP^{TSE} comprised 95% of the stainable components in the preparations, not accounting for poor staining of glycoproteins such as PrP. Transmission electron microscopy of purified preparations showed the presence of the archetypical bundles of PrP^{TSE} fibrils (Fig. S2). Individual fibrils were typically 10–14 nm in diameter and 75–125 nm in length, consistent with previous reports.³⁹ Differences between aggregate structures of PrP^{TSE} and PrP^{27–30} were not readily discernable. Protein concentrations in each preparation were determined after denaturation by the bicinchoninic acid assay. Redundant standard curves were prepared using Syrian hamster recPrP (>95%; Jena BioScience, Jena, Germany) and high purity bovine serum albumin (>99%; Sigma-Aldrich) (see SI for details). Recombinant mouse PrP (recMoPrP, residues 90–230) was generously provided by Dr. Giuseppe Legname.

Electrophoretic Mobility and Diffusivity Measurements

The electrophoretic mobility (μ_e) and diffusivity (D_w) of PrP^{TSE} and PrP^{27–30} aggregates in water at $24.0 \pm 0.1^\circ\text{C}$ were measured by electrophoretic light scattering (ELS) and dynamic light scattering (DLS) with a Malvern ZetaSizer Nano ZS (Worcestershire, UK). Purified PrP preparations, diluted to final protein concentrations of $500 \text{ ng}\cdot\text{mL}^{-1}$ and $5.0 \text{ }\mu\text{g}\cdot\text{mL}^{-1}$ in buffers of desired pH and *I*, were used for ELS and DLS experiments, respectively. Prior to measurement, PrP solutions were vortexed briefly and sonicated (1 min; Branson 2510 sonic

bath, Branson Ultrasonics, Danbury, CT), and equilibrated for 10 min prior to the first measurement. The mean values and standard deviations reported represent the average of five measurements performed on each of five solutions (25 total measurements). Time-resolved μ_e and D_w measurements were made over 45 min to assess changes in these parameters on time scales relevant for attachment experiments. Instrument performance was periodically verified with polymer microsphere standards of known μ_e and D_w (DTS1235, Malvern).

Preparation of Surfaces

To ensure the comparability of the surfaces used in QCM-D and OWLS experiments, QCM-D sensors and OWLS waveguides were custom coated. Gold-coated QCM-D sensors (QSX301, Biolin Scientific, Göteborg, Sweden) and SiTi₃O₈ OWLS waveguides (OW2400, MicroVacuum, Budapest, Hungary) were coated with amorphous silicon dioxide (SiO₂) by plasma-enhanced chemical vapor deposition (GeSiM mbH, Großerkmannsdorf, Germany) or amorphous aluminum oxide (Al₂O₃) by spin coating (Aluminafilm, Emulsitone Company, Whippany, NJ). Coating thickness was determined by edge-on scanning electron microscopy (Supra 55VP, LEO, Cambridge, UK) to be 50 nm for the QCM-D sensors and 12 nm for the waveguides. The points of zero charge (pzc) for SiO₂ and Al₂O₃ were respectively 3.5⁴⁰ and 7.50–7.75 (the latter determined by attachment of negatively charged citrate-TiO₂ nanoparticles; see SI). Sensors were rigorously cleaned prior to each experiment (see SI).

We electrostatically assembled poly-L-lysine (PLL) films *in situ* on SiO₂-coated QCM-D sensors (QSX303) and OWLS waveguides (2400c) to produce an additional positively charged surface (pH_{IEP} = 9–9.8)⁴¹. To accomplish this, we pumped a 100 µg·mL⁻¹ PLL (M_r = 70,000–150,000, Sigma-Aldrich, St. Louis, MO) solution with the same composition as used for the subsequent protein attachment experiment over the sensors for 10 min followed by 10-min rinsing with PLL-free solution to remove any free or loosely bound PLL.

Attachment Experiments

We conducted QCM-D experiments using a Q-Sense E4 instrument (Biolin Scientific) containing four sensors mounted in flow cells that achieve a completely laminar liquid flow across the sensor surface. Temperature was maintained at 24.0 ± 0.5 °C. In QCM-D, an AC voltage imposed across an AT-cut piezoelectric quartz crystal causes it to vibrate in shear mode at its resonance frequency (fundamental resonance frequency, $f_1 \approx 4.95$ -MHz for the crystals used here). Changes in the resonance frequency (f) correspond to changes of mass ($m_{\text{QCM-D}}$) on the quartz crystal surface. The sensed mass includes both analyte molecules and hydrodynamically coupled water. The driving voltage to the crystal is periodically switched off (5 s^{-1}), and the energy dissipation (D) determined. More viscoelastic layers dampen vibrations more efficiently than do more rigid layers and thus produce larger dissipation values.⁴² For rigid adlayers (usually defined as having a D -to- f ratio $\ll 0.4 \times 10^{-6}$),⁴³ f is directly proportional to adlayer mass, and attached surface mass density can be calculated with the Sauerbrey equation.⁴⁴ For more dissipative adlayers (i.e., those not completely coupled to the vibrations of the quartz sensor), this direct relationship no longer holds. For laterally homogeneous adlayers, surface mass density can be estimated by

continuum viscoelastic modeling if adlayer density and bulk fluid viscosity and shear modulus are known.^{43,45} The QCM-D instrument simultaneously monitors f and D at the fundamental ($i=1$) and odd overtones ($i=3$ to 11). Changes in dissipation and the normalized frequency are reported for the 5th overtone (~25 MHz) unless otherwise noted. All f data used to determine initial attachment rates ($k_{\text{QCM-D}}$) were subjected to locally weighted scatterplot smoothing (LOESS)⁴⁶ with a smoothing parameter of 0.1 (see the SI for details).

The D_i and f_i data ($i=1-11$, odd overtones) from selected QCM-D runs were fit to a Kelvin-Voigt viscoelastic model⁴⁵ using QTools software (Version 3.0, Biolin Scientific) in the manner of Eisele et al.⁴⁷ The bulk liquid phase was assumed to be a Newtonian fluid with a density of 0.997 kg·m⁻³ and dynamic viscosity of 0.93 mPa·s⁻¹. The models were fit to minimize differences between measured data and model outputs by stepwise alteration of the input adlayer density.

We conducted OWLS experiments using an OWLS 210 instrument (MicroVacuum) containing a single sensor mounted in a laminar slit shear-flow cell. The temperature was maintained at 24.0±0.2°C. In OWLS, linearly polarized He-Ne laser light (632.8nm) is guided through a diffraction grating etched into waveguide surface and changes in the phase velocities of the transverse magnetic and transverse electric signals are monitored.⁴⁸ Analyte adsorption to the surface causes changes in phase velocities that can be related to (optical) adlayer thickness (d_A) and refractive index (n_A).⁴⁹ Surface concentrations of molecules (areal mass densities) can be derived using de Feijter's formula:⁵⁰

$$m_{\text{OWLS}} = d_A \frac{n_A - n_C}{dn/dC} \quad (1)$$

where m_{OWLS} is the areal mass density determined by OWLS (g·cm⁻²); n_C is the refractive index of the buffer solution; and dn/dC is the refractive index increment of the adlayer molecules (cm⁻³·g). Refractive indices of the buffers used (n_C) were determined at 24.0 °C using a refractometer with a 632.8-nm He-Ne laser (Model J157-633, Rudolph Research, Hackettstown, NJ) and are reported in the SI. The refractive index increment (dn/dC) was taken to be 0.182 g·cm⁻³, the generally accepted value for proteinaceous material.⁵¹

Solutions used in QCM-D and OWLS experiments were buffered to the desired pH with 3 mM acetate (pH 4 and 5), 2-(*N*-morpholino) ethanesulfonic acid (MES; pH 6), 4-(2-hydroxyethyl)-1-piperazineethanesulfonic acid (HEPES; pH 7 and 8), or *N*-cyclohexyl-2-aminoethanesulfonic acid (CHES; pH 9), and I was adjusted with NaCl. All solutions were passed through a 0.1-μm polyvinylidene fluoride filter (Millipore, Billerica, MA) and ultrasonically degassed prior to use.

Attachment experiments commenced with flowing protein-free buffer solution across the cleaned sensor crystal or waveguide to allow equilibration as evidenced by attainment of a stable baseline signal (defined for QCM-D as $df_5 \cdot dt^{-1} < 0.05$ Hz·min⁻¹ and for OWLS as a rate of change of the effective refractive indices for the transverse electric and transverse magnetic polarizations ($dN_{\text{TE}} \cdot dt^{-1}$ and $dN_{\text{TM}} \cdot dt^{-1}$, respectively) $< 10^{-8}$ min⁻¹). A 5.0±0.1 μg·mL⁻¹ solution of purified PrP (representing a 1:160 to 1:300 dilution of stock

preparations) was then introduced into the flow cell. Immediately prior to introduction into the QCM-D or OWLS, the diluted protein solution was briefly mixed by vortexing and sonicated for 1 min (Branson 2510 sonic bath). For most QCM-D experiments, protein solution was flowed across the sensor surface for 40 min, followed by rinsing with protein-free solution (40 min) to examine the attachment reversibility. Due to the lower temporal resolution of OWLS measurements (sampling frequency=0.07–0.1 s⁻¹), the difficulty obtaining purified PrP, and the excellent agreement between OWLS and QCM-D experiments,^{52,53} OWLS experiments were conducted for only selected conditions. A flow rate of 50±3 μL·min⁻¹ was maintained for all stages of all experiments using a peristaltic pump (ISMATEC IPC, IDEX, Oak Harbor, Washington). This flow rate was determined to produce diffusion-controlled attachment rates under all solution conditions used.

Initial prion attachment rates, k_{oxide} were estimated from $f_5/5$ data by calculating the average of the 1-min slopes from 1 to 5 min after protein introduction to the sensor chamber. The first minute of attachment was excluded to ensure calculated rates did not include data points prior to the bulk fluid protein concentration reaching steady state. Attachment efficiencies (α), defined as the fraction of protein-surface encounters resulting in attachment relative to transport-limited case, were calculated as the ratio of the initial rate of attachment to the surface of interest to that for a totally electrostatically favorable surface:

$$\alpha = \frac{k_{\text{oxide}}}{k_{\text{PLL}}} \quad (2)$$

where k_{oxide} is the initial attachment rate to a given oxide surface (Hz·min⁻¹), and k_{PLL} is that to PLL under the same solution conditions.

Atomic Force Microscopy (AFM)

Prion fibrils attached to Al₂O₃-coated QCM-D sensors were imaged with a Multimode IV AFM (Bruker, Santa Barbara, CA). Sensors from three experimental time points were examined: prior to protein introduction, after 5 min of protein attachment, and after the areal mass density had attained a plateau. Prior to removal from the flow cell, sensors were rinsed with protein-free background solution to rinse any loosely bound fibrils from the surface. Both topographical (height variations in the scanned area) and phase data (lag between the phase recorded by the oscillating cantilever and that of the signal sent by the piezoelectric controller) was collected.⁵⁴ Use of both types of imaging aids visualization of dissimilar materials because contrast between materials differing in softnesses and viscoelasticity (e.g., oxides and biomolecules) is dramatically enhanced in phase data. For selected regions, the height of objects above sensor surfaces and the root mean squared roughness (R_{RMS}) was calculated using Nanoscope Analysis, Ver8.0 (Bruker). See the SI for details.

RESULTS AND DISCUSSION

Properties of PrP Fibrils

Electrophoretic Mobilities—Prion fibrils (both PrP^{TSE} and PrP^{27–30}) exhibited net negative charge over the pH range examined (pH 4–9) and were strongly negatively charged over the pH and ionic strength range used in attachment experiments (Figure 1a).

Electrophoretic mobilities of prion fibrils became more negative as pH increased, consistent with the progressive deprotonation of acidic and basic amino acid side chains. For pH 5, μ_e was less negative at $I = 50$ mM than at 5 mM due to charge screening. At the lower ionic strength, μ_e values for PrP^{27–30} were more negative than for PrP^{TSE} at pH 5–8. This difference is not apparent at the higher ionic strength. The higher net negative charge for PrP^{27–30} relative to PrP^{TSE} is due to the presence of 10 basic amino acid residues (3 Lys, 3-Arg, 4 His) in the PK-sensitive N-terminus of the protein, absent in PrP^{27–30}. The μ_e values were negative over the pH range examined, despite the primary structure of PrP containing more basic than acidic amino acid residues. This is due to the presence of sialic acid residues ($pK_a = 2.5$)⁵⁵ in the N-linked glycans⁵⁶ and glycosylphosphatidylinositol anchors,⁵⁷ and tertiary and quaternary structure of the protein. Apparently, the folding of pathogenic conformer and its assembly into fibrils results in exposure of more negatively than positively charged amino acid side chains to solution. The μ_e values for PrP^{TSE} were slightly more negative than those reported previously for PrP^{TSE} fibrils purified using a slightly different protocol.²⁹

Diffusivities—The diffusivities of PrP^{TSE} and PrP^{27–30} fibrils in water (D_w) were higher at lower I (Figure 1b), indicating smaller aggregate size. The decrease in D_w at higher I is attributable to double layer compression and aggregation. Diffusivities varied little if at all over the pH range examined (pH 6–9). Differences in D_w between PrP^{27–30} and PrP^{TSE} samples under the identical solution conditions were small or nonexistent. This suggests that, although the PrP^{27–30} aggregates possess a higher net negative charge, any decrease in aggregation due to increased electrostatic repulsion were not large enough to be observable using DLS. Diffusivities for PrP^{TSE} and PrP^{27–30} in all solutions used were stable over the time period of typical attachment experiments (data not shown), implying that the average aggregation state of the protein did not change appreciably over the course of attachment experiments. Similar D_w values were observed in a previous study of the solution properties of prion aggregates.²⁹

Comparison of QCM-D and OWLS Data

Figure 2a displays representative QCM-D data for the attachment of PrP^{27–30} to an Al₂O₃ surface at pH 6 and $I = 5$ mM. Prior to protein introduction into the flow cell ($t < 0$), the f_i/i and D_i curves for all overtones were tightly grouped at or near 0. Upon introduction of PrP^{27–30} ($t = 0$), the f_i/i curves begin to decrease, indicating deposition of mass. The initial rate of change (df_i/dt^{-1}) in this example is equivalent to the diffusion-limited rate as determined by attachment to a PLL-coated sensor. The rate of attachment slowly declines as available areas on the sensor surface become occupied with PrP^{27–30} and df_i/dt^{-1} approaches 0 Hz·min⁻¹ at $t = 146$ min. The D_i curves follow the opposite trend, increasing as f_i decreases. The large D_i values obtained indicate the PrP^{27–30} adlayer is highly dissipative. Pronounced overtone dispersion occurred for both f_i/i and D_i . After the f_i/i values approached plateaus, protein-free buffer solution with the same pH and I was introduced into the flow cell to examine the reversibility of attachment. During rinsing, a small increase in f_i/i (0.2–0.5 Hz) was observed, indicating a loss of mass coupled to the sensor.

In Figure 2b we plot the areal mass density detected by the QCM-D ($m_{\text{QCM-D}}$) as a function of time from the data in Figure 2a. We calculated $m_{\text{QCM-D}}$ using a continuum viscoelastic model⁴⁵ as described above. Also included in Figure 2b is the areal mass density as determined by OWLS (m_{OWLS}) for PrP²⁷⁻³⁰ attachment to Al₂O₃ under the same solution conditions. The $m_{\text{QCM-D}}$ and m_{OWLS} plots exhibit initial rates of PrP²⁷⁻³⁰ attachment to the Al₂O₃ surface at or near the diffusion-limited rate before slowing and reaching stable values. The OWLS data confirm that the protein-free buffer rinse produced a small (3–8 ng·cm⁻²), but measurable, amount of detachment. The mass loss corresponded to 1–2% of the PrP²⁷⁻³⁰ areal mass density prior to rinsing. The large difference between $m_{\text{QCM-D}}$ and m_{OWLS} is due to hydrodynamically coupled water sensed by QCM-D but not OWLS. Below we discuss the initial kinetics of pathogenic PrP attachment to Al₂O₃ and SiO₂, PrP detachment, and the properties of the fully formed PrP adlayer.

Initial Attachment Kinetics

The difficulty in obtaining large quantities of pathogenic PrP led us to focus the bulk of our analyses on initial attachment kinetics. We relied on QCM-D for these experiments. Attachment efficiencies for PrP^{TSE} and PrP²⁷⁻³⁰ interaction with Al₂O₃ and SiO₂ surfaces are displayed in Figures 3a and b, respectively. The numerical data are given in Tables S3 and S4. Over the pH range examined (pH 6–9), PrP^{TSE} and PrP²⁷⁻³⁰ possess net negative charge. The Al₂O₃ surface is net positively charged below its apparent pzc of 7.50–7.75, and negatively charged above this point. The SiO₂ carries a net negative charge over the entire pH range (pzc=3.5). Surface charge densities reported for similar surfaces over the same pH range are +0.04 to –0.01 C·m⁻² for γ -Al₂O₃ and –0.02 to –0.06 C·m⁻² for am-SiO₂.⁴⁰ Reported Hamaker coefficients for α -Al₂O₃ and am-SiO₂ are 3.67 and 0.46×10^{-20} J, respectively.⁵⁸

Al₂O₃ Surfaces—At the relatively low ionic strength of 5 mM (Debye length, $\kappa^{-1} = 4.3$ nm), attachment efficiencies were near 1.0 for pH values at which the Al₂O₃ surface was positively charged. For pH values above the apparent pzc, α values decreased to 0.04 to 0.10. Increasing I to 50 mM ($\kappa^{-1}=1.4$ nm) resulted in α values near 1.0 for pH < pzc for both PrP^{TSE} and PrP²⁷⁻³⁰ attaching to Al₂O₃. For pH > pzc, raising I produced an increase in α consistent with screening of electrostatic repulsion. At these pH values and $I = 50$ mM, $\alpha \approx 1$ for PrP^{TSE}, while those for PrP²⁷⁻³⁰ were somewhat lower (0.64 and 0.44 for pH 8 and 9). Despite carrying a net negative charge at these pH values, reported charge densities for aluminum oxides over this pH range are lower than those for SiO₂ by a factor of ~ 5 .⁴⁰ These results are consistent with predictions from classical DLVO theory: attachment occurs near the diffusion-limited rate under electrostatically favorable conditions (pH < pzc); and at pH > pzc, increasing I diminishes the magnitude and range of electrostatic repulsion while attractive van der Waals forces remain essentially unaltered leading to more favorable attachment conditions. The larger α for PrP^{TSE} vis-à-vis PrP²⁷⁻³⁰ may be due to the larger size and less negative surface charge of the PrP^{TSE} aggregates leading to an overall increase in attraction, interaction of the N-terminal portion of the protein present in PrP^{TSE} with the surface (by providing more points of contact with the surface or reducing the energy barrier to attachment),⁵⁹ or both

SiO₂ Surfaces—At $I = 5$ mM, α values for both forms of pathogenic PrP were < 0.1 . Attachment efficiencies did not vary with pH for PrP^{TSE} from pH 6 to 7 and for PrP^{27–30} from 6 to 8. At higher pH values, α declined. While α values were small for both types of protein, attachment efficiencies for PrP^{TSE} were lower than those for PrP^{27–30} and at pH 8–9 were close to the limit of detection (see-SI) consistent with strong electrostatic repulsion between the similarly charged fibrils and SiO₂ surface. Relative to PrP^{27–30}, the larger size of PrP^{TSE} leads to increased van der Waals attraction, but to a much smaller extent than for Al₂O₃ due to the much lower Hamaker coefficient of SiO₂. The increase in electrostatic repulsion due to the increase in aggregate size was partially offset by the decrease in apparent ζ -potential. The relative magnitudes of the changes in van der Waals and electrostatic double layer interactions appears to have led to an overall increase in the energy barrier for attachment to SiO₂ for PrP^{TSE} relative to PrP^{27–30}. Increasing I to 50 mM resulted in a clear increase in α for PrP^{TSE} over the entire pH range examined due to screening of repulsive electrostatic interactions; α declined with pH consistent with the increasing negative charge of PrP^{TSE} (Figure 1a) and the SiO₂ surface. Interestingly, for PrP^{27–30}, the increase in I produced the expected increase in α only at pH 6. The reason for the lack of significant increase in α at higher pH values is not clear but would appear to be related to the lack of the N-terminus. The general trends observed for PrP^{TSE} attachment to SiO₂ are consistent with classical DLVO theory: electrostatic repulsion increases as both the protein and the SiO₂ surface become more negatively charged with increasing pH and decreases as ionic strength is raised. At pH 8 and 9, the low α values for attachment to SiO₂ contrast with those for Al₂O₃ and are consistent with the higher charge density of SiO₂ at these proton activities (see above) and the larger Hamaker coefficient for Al₂O₃.

Detachment of Prion Fibrils

Attachment of PrP^{TSE} and PrP^{27–30} fibrils to Al₂O₃ surfaces was irreversible with respect to dilution (e.g., Figure 1). In QCM-D experiments, frequency shifts occurring during rinsing the PrP adlayer with protein-free buffer were $\sim 1\%$ and did not depend on pH, I , or type of PrP (viz. PrP^{TSE} or PrP^{27–30}). Similar amounts of detachment were observed for experiments in which the attachment plateau was attained and those halted at earlier stages in adlayer evolution. Mass losses in corresponding OWLS experiments were 5–10 ng·cm⁻² (3–7%; data not shown) Similar results were obtained for attachment to SiO₂ surfaces. Rinsing produced increases in f_i of similar magnitude for the two surfaces. Due to the much lower f_i obtained on the SiO₂ surfaces, the decrease in mass coupled to the sensor represented a larger fraction of the mass associated with the surface at the end of the attachment period. For SiO₂, maximal frequency shifts were $\sim 30\%$ of the final value. Mass losses in parallel OWLS experiments were 2–4 ng·cm⁻² (10–30%; data not shown) upon rinsing. As in Al₂O₃ experiments, no obvious trend was observed for prion detachability with respect to solution chemistry or N-terminal truncation of the protein. Reversing the net charge on the oxide surface was unable to completely detach a fully formed PrP^{27–30} adlayer; rinsing an adlayer deposited on Al₂O₃ at pH 6 with pH 8 buffer ($I = 5$ mM) caused only small net increases in f_i ($\sim 10\%$; data not shown). At a pH of 8, Al₂O₃ carries a very low net negative charge density,⁴⁰ which provides insufficient repulsive force to overcome the van der Waals interactions and hydrogen bonds at multiple points of contact between prion aggregates and the surface.

Fully Formed Adlayer

Under selected conditions, QCM-D and OWLS experiments were allowed to proceed until fully formed PrP²⁷⁻³⁰ adlayers developed. Such experiments demanded large quantities of pathogenic PrP; each experiment required the amount of purified PrP from two or more hamster brains. Conducting such experiments for the full complement of solution conditions, surfaces, and types of pathogenic PrP would have been prohibitively costly. Plots of the QCM-D and OWLS data are presented in Figures S4 and S5.

To visualize PrP²⁷⁻³⁰ adlayer development, we acquired topographical and phase images by tapping mode AFM for bare Al₂O₃ sensors, the developing PrP²⁷⁻³⁰ adlayer, and the fully formed adlayer (Figure 4). The bare Al₂O₃ was relatively smooth with a root mean square roughness, $R_{\text{RMS}} = 1.5 \pm 0.14$ nm. AFM images of the developing adlayer (Figure 4c,d) exhibit distinct fibrillar objects of varying size distributed across the Al₂O₃ surface. These objects include small, single fibrils and large clumps of aggregated fibrils. The heights of the small fibrils were between 11 and 15 nm, similar to diameters determined by TEM. The heights of larger clumps of fibrils on the surface were in some cases as large as 60 nm. The presence of large clumps on the surface may indicate that adlayer formation proceeds in part by surface aggregation, but more highly temporally resolved data would be needed to be confident of this interpretation. For the fully developed adlayer (Figure 4e,f), the Al₂O₃ surface was covered with a mat of fibril-like structures with $R_{\text{RMS}} = 16 \pm 1.0$ nm. The surface topology shows variability in mat height with a maximum top to bottom difference of ~60 nm.

The lateral homogeneity of the fully developed PrP²⁷⁻³⁰ adlayers on Al₂O₃ surfaces at pH 6 and 7 at $I = 5$ mM appeared sufficient to permit Kelvin-Voigt continuum viscoelastic modeling of the QCM-D data. The small plateau values for f for PrP²⁷⁻³⁰ adlayers on SiO₂ under the same solution conditions (Table 1) indicated that the protein layers on these sensors were not likely laterally homogenous and thus not suitable for viscoelastic modeling. The viscoelastic modeling results as well as the thicknesses and masses of the fully developed adlayers as measured by OWLS are displayed in Table 1. The fully developed adlayer formed at pH 6 was thicker but had similar protein density to the one formed at pH 7. The fully developed adlayers on Al₂O₃ contained ~98% water.

The trends in attached masses as a function of solution chemistry for the am-SiO₂ surfaces employed in the QCM-D and OWLS experiments are congruent with those reported previously for quartz using batch and column attachment techniques and PrP^{TSE} purified in slightly different manner.²⁹ Such congruence between more traditional techniques and QCM-D and OWLS was recently highlighted in a study examining adsorption of transgenic insecticidal crystal (Cry) proteins derived from *Bacillus thuringiensis* to SiO₂.⁶⁰ The areal surface densities for pathogenic PrP attaching to SiO₂ in the present study were lower than those previously reported by Johnson et al.²⁷ This discrepancy is likely due primarily to limitations in the detection method applied in the earlier study. We find that solution chemistry strongly impacts prion attachment to SiO₂ surfaces. This contrasts with an earlier study reporting a limited effect of solution chemistry on attachment to quartz when brain homogenate was used as the prion source.⁶¹ Brain homogenate contains a complex mixture

of proteins, lipids, and other biomolecules in quantities far exceeding that of PrP, thus preventing the investigating of direct interactions of pathogenic PrP with surfaces as done in the present study.

Evaluation of Recombinant PrP as a Surrogate for PrP^{TSE}

The difficulty in obtaining pathogenic PrP and its infectious nature has motivated interest in using surrogates for PrP^{TSE} in environmental studies. Several published studies have employed prokaryotically expressed recPrP to circumvent the difficulties in working with infectious agent.^{62–65} We therefore investigated the extent to which recombinant mouse PrP (recMoPrP, 95% sequence homology with Syrian hamster PrP⁶⁶; none of the amino acid substitutions involve acidic or basic residues) attachment to Al₂O₃ and SiO₂ was similar to that of *bona fide* PrP^{TSE}. We made this comparison at pH 6, $I = 5$ mM.

The attachment behavior of recMoPrP differed dramatically from that of PrP^{27–30} under the tested solution conditions (Figure S3). Relative to PrP^{27–30}, recMoPrP attachment to Al₂O₃ was much reduced ($f_{5\text{plateau}}/5_{\text{Al}_2\text{O}_3} = -2.8$ and -248 Hz for recMoPrP and PrP^{27–30}) and that to SiO₂ was markedly increased ($k_{\text{SiO}_2} = -17$ and -1.4 Hz for recMoPrP and PrP^{27–30}). Unlike PrP^{27–30}, changes in dissipation (D_i) were very small ($<0.3 \times 10^6$). Plotting D_5 against f_5 for recMoPrP and PrP^{27–30} attachment to these surfaces highlights the striking differences attachment behavior (Figure S3). RecMoPrP behaves like other small, monomeric proteins that form a thin rigid adlayer on surfaces, particularly those that it is electrostatically attracted to ($pI_{\text{recMoPrP}} = 9.4$). These results indicate that recMoPrP cannot be used as a surrogate to understand the attachment of pathogenic PrP to environmental surfaces.

Environmental Implications

The fate, transport, and bioavailability of prions in soil and sediment environments are expected to depend in part on the interactions of these proteins with oxide surfaces. Soils and sediments are complex natural systems, and prion behavior in these matrices depends on their interaction with the various constituents of these systems and their combinations. The present study using model surfaces contributes to the understanding of the interfacial processes governing protein interaction with oxide surfaces. Our findings suggest that prions released into soil environments would tend to associate with positively charged mineral surfaces such as gibbsite ($\gamma\text{-Al(OH)}_3$; $pzc=10.0$),⁶⁷ goethite ($\alpha\text{-FeOOH}$; $pzc = 8.1$),⁶⁸ hematite ($\alpha\text{-Fe}_2\text{O}_3$; $pzc = 8.5$),⁴⁰ and ferrihydrite ($\text{Fe}_5\text{HO}_8 \cdot 4\text{H}_2\text{O}$; $pzc=8.0$).⁶⁹ Our results show that attachment is not insignificant to low charge-density oxide surfaces under electrostatically repulsive conditions. Surface soil composition and pore water chemistry are expected to influence retention of prions near the soil surface. Prions retained by particles at the soil surface may be subject to transport to surface waters.⁷⁰ Prion association with natural organic matter material has not been formally examined and warrants investigation. Recent work has indicated the importance of adsorption to humic substances for the insecticidal Cry1Ab protein.⁷¹

Supplementary Material

Refer to Web version on PubMed Central for supplementary material.

Acknowledgments

We thank Istvan Szendro and Mark Poggi for helpful discussions, Joe Yeager for SEM assistance, Steffen Horowitz for assistance with vapor deposition, and Julie Last for assistance with AFM. This work was supported by National Science Foundation grants CBET-0826204 (prion experiments) and DRM-0832760 (TiO₂ nanoparticle experiments). This paper is part of a tribute issue honoring René P. Schwarzenbach for his many influential contributions to environmental organic chemistry.

LITERATURE CITED

1. Miller MW, Williams ES, Hobbs NT, Wolfe LL. Environmental sources of prion transmission in mule deer. *Emerg Infect Dis*. 2004; 10:1003–1006. [PubMed: 15207049]
2. Schramm PT, Johnson CJ, Mathews NE, McKenzie D, Aiken JM, Pedersen JA. Potential role of soil in the transmission of prion disease. *Medical Mineralogy and Geochemistry. Rev Mineral Geochem*. 2006; 64:135–152.
3. Pedersen, JA.; Somerville, R. Why and how are TSEs sometimes spread via environmental routes?. In: Deslys, J-P.; Pocchiari, M.; Reisner, D.; Somerville, R., editors. *Decontamination of Prions*. Düsseldorf University Press; Düsseldorf, Germany: 2012. p. 19-37.
4. Pruisner SB. Prions. *Proc Natl Acad Sci USA*. 1998; 95:13363–13383. [PubMed: 9811807]
5. Peralta OA, Eyestone WH. Quantitative and qualitative analysis of cellular prion protein (PrP^C) expression in bovine somatic tissues. *Prion*. 2009; 3:161–170. [PubMed: 19806026]
6. Brown P, Cervenakova L. A prion lexicon (out of control). *Lancet*. 2005; 365:122. [PubMed: 15639292]
7. Safar J, Roller PP, Gajdusek DC, Gibbs CJ Jr. Scrapie amyloid (prion) protein has the conformational characteristics of an aggregated molten globule folding intermediate. *Biochem*. 1994; 33:8375–8383. [PubMed: 8031772]
8. Smirnovas V, Baron GS, Offerdahl DK, Raymond GJ, Caughey B, Surewicz WK. Structural organization of brain-derived mammalian prions examined by hydrogen-deuterium exchange. *Nature Struct Molec Biol*. 2011; 18:504–506. [PubMed: 21441913]
9. Gossert AD, Bonjour S, Lysek DA, Fiorito F, Wüthrich K. Prion protein NMR structures of elk and of mouse/elk hybrids. *Proc Natl Acad Sci US A*. 2005; 102:646–650.
10. Lysek DA, Schorn C, Nivon LG, Esteve-Moya V, Christen B, Calzolari L, von Schroetter C, Fiorito F, Herrmann T, Guntert P, Wüthrich K. Prion protein NMR structures of cats, dogs, pigs, and sheep. *Proc Natl Acad Sci US A*. 2005; 102:640–645.
11. Reik R, Hornemann S, Wider G, Glockshuber, Wüthrich K. NMR characterization of the full-length recombinant murine prion protein, mPrP(23–231). *FEBS Lett*. 1997; 413:282–288. [PubMed: 9280298]
12. Zahn R, Liu A, Lührs T, Riek R, von Schroetter C, López Garcia F, Billeter M, Calzolari L, Wider G, Wüthrich. NMR solution structure of the human prion protein. *Proc Natl Acad Sci USA*. 2000; 97:145–150. [PubMed: 10618385]
13. Colby DW, Pruisner SB. Prions. *Cold Spring Harb Perspect Biol*. 2011; 3:a006833. [PubMed: 21421910]
14. DeMarco ML, Silveira J, Caughey B, Dagget V. Structural properties of prion protein protofibrils and fibrils: An experimental assessment of atomic models. *Biochem*. 2006; 45:15573–15582. [PubMed: 17176078]
15. Diaz-Espinoza R, Soto C. High-resolution structure of infectious prion proteins: the final frontier. *Nature Struct Molec Biol*. 2012; 19:370–377. [PubMed: 22472622]
16. Tamgüney G, Miller MW, Wolfe LL, Sirochman TM, Glidden DV, Palmer C, Lemus A, DeArmond SJ, Pruisner SB. Asymptomatic deer excrete infectious prions in faeces. *Nature*. 2009; 461:529–532. [PubMed: 19741608]

17. Tamgüney G, Miller MW, Wolfe LL, Sirochman TM, Glidden DV, Palmer C, Lemus A, DeArmond SJ, Prusiner SB. Asymptomatic deer excrete infectious prions in faeces. *Nature*. 2009; 466:652.
18. Gregori L, Kovacs GG, Alexeeva I, Budka H, Rohwer RG. Excretion of transmissible spongiform encephalopathy infectivity in urine. *Emerg Infect Dis*. 2008; 14:1406–1412.
19. Mathiason CK, Powers JG, Dahmes SJ, Osborn DA, Miller KV, Warren RJ, Mason GL, Hays SA, Hayes-Klug J, Seelig DM, Wild MA, Wolfe LL, Spraker TR, Miller MW, Sigurdson CJ, Tellings GC, Hoover EA. Infectious prions in the saliva and blood of deer with chronic wasting disease. *Science*. 2006; 314:133–136. [PubMed: 17023660]
20. Brown P, Gajdusek DC. Survival of scrapie virus after 3 years' interment. *Lancet*. 1991; 337:269–270. [PubMed: 1671114]
21. Seidel B, Thomzig A, Buschmann A, Groschup MH, Peters R, Beekes M, Terytze K. Scrapie agent (strain 263K) can transmit disease via the oral route after persistence in soil over years. 2007; 5:e435.
22. Arthur WJ III, Alldredge AW. Soil ingestion by mule deer in northcentral Colorado. *J Range Manage*. 1979; 32:67–71.
23. Beyer WN, Conner EE, Gerould S. Estimates of soil ingestion by wildlife. *J Wildl Manage*. 1994; 58:375–382.
24. Hui CA. Geophagy and potential contaminant exposure for terrestrial vertebrates. *Rev Environ Contam Toxicol*. 2004; 183:115–134. [PubMed: 15369324]
25. Johnson CJ, Pedersen JA, Chappell RJ, McKenzie D, Aiken JM. Oral transmissibility of prion disease is enhanced by binding to soil particles. *PLoS Path*. 2007; 3:e93.
26. Johnson CJ, McKenzie D, Pedersen JA, Aiken JM. Meat and bone meal and mineral feed additives may increase the risk of oral prion disease transmission. *J Toxicol Environ Health A*. 2011; 74:161–166. [PubMed: 21218345]
27. Johnson CJ, Phillips KE, Schramm PT, McKenzie D, Aiken JM, Pedersen JA. Prions adhere to soil minerals and remain infectious. *PLoS Path*. 2006; 2:e32.
28. Cooke CM, Shaw G. Fate of prions in soil: Longevity migration of recPrP in soil columns. *Soil Biol Biochem*. 2007; 39:1181–1191.
29. Ma X, Benson CH, McKenzie D, Aiken JM, Pedersen JA. Adsorption of pathogenic prion protein to quartz sand. *Environ Sci Technol*. 2007; 41:2324–2330. [PubMed: 17438782]
30. Hinckley GT, Johnson CJ, Jacobson KH, Bartholomay C, McMahan KD, McKenzie D, Aiken JM, Pedersen JA. Persistence of pathogenic prion protein during simulated wastewater treatment processes. *Environ Sci Technol*. 2008; 42:5254–5259. [PubMed: 18754377]
31. Jacobson KH, Lee S, McKenzie D, Benson CH, Pedersen JA. Transport of the pathogenic prion protein through landfill materials. *Environ Sci Technol*. 2009; 43:2022–2028. [PubMed: 19368208]
32. Saunders SE, Bartz JC, Bartelt-Hunt SL. PrP adsorption to soil in a competitive matrix is slow and reduced. *Environ Sci Technol*. 2009; 43:7728–7733. [PubMed: 19921886]
33. Jacobson KH, Lee S, Sommerville RA, McKenzie D, Benson CH, Pedersen JA. Transport of the pathogenic prion protein through soils. *J Environ Qual*. 2010; 39:1145–1152. [PubMed: 20830901]
34. Maddison BC, Owen JP, Bishop K, Shaw G, Rees HC, Gough KC. The interaction of ruminant PrP^{Sc} with soils is influenced by prion source and soil type. *Environ Sci Technol*. 2010; 44:8503–8508. [PubMed: 20968294]
35. Saunders SE, Bartz JC, Telling GC, Bartelt-Hunt SL. Environmentally relevant forms of the prion protein. *Environ Sci Technol*. 2008; 42:6573–6579. [PubMed: 18800532]
36. Bessen RA, Marsh RF. Distinct PrP properties suggest the molecular basis of strain variation in transmissible mink encephalopathy. *J Virol*. 1994; 68:7859–7868. [PubMed: 7966576]
37. Raymond, GJ.; Chabry, J. Purification of the pathological isoform of prion protein (PrP^{Sc} or PrP^{Res}) from transmissible spongiform encephalopathy-affected brain tissue. In: Lehmann, S.; Grassi, J., editors. *Techniques in Prion Research*. Birkhäuser Verlag; Basel: 2004. p. 16-26.

38. Cronier S, Gros N, Tattum MH, Jackson GS, Clarke AR, Collinge J, Wadsworth JDF. Detection and characterization of proteinase K-sensitive disease-related prion protein with thermolysin. *Biochem J.* 2008; 416:297–305. [PubMed: 18684106]
39. Prusiner SB, McKinley MP, Bowman KA, Bolton DC, Bendheim PE, Groth DF, Glenner GG. Scrapie prions aggregate to form amyloid-like birefringent rods. *Cell.* 1983; 35:349–358. [PubMed: 6418385]
40. Sahai N, Sverjensky DA. Evaluation of internally consistent parameters for the triple-layer model by the systematic analysis of oxide surface titration data. *Geochim Cosmochim Acta.* 1997; 61:2801–2826.
41. Lundblad, RL.; MacDonald, F. *Handbook of Biochemistry and Molecular Biology.* CRC Press; Boca Raton: 2010.
42. Rodahl M, Höök F, Krozer A, Brzezinski P, Kasemo B. Quartz crystal microbalance setup for frequency and Q-factor measurements in gaseous and liquid environments. *Rev Sci Instrum.* 1995; 66:3924–3930.
43. Reviakine I, Johannsmann D, Richter RP. Hearing what you cannot see and visualizing what you hear: Interpreting quartz crystal microbalance data from solvated interfaces. *Anal Chem.* 2011; 83:8838–8848. [PubMed: 21939220]
44. Sauerbrey G. Verwendung von Schwingquarzen zur Wägung dünner Schichten und zur Mikrowägung. *Z Phys.* 1959; 155:206–222.
45. Voinova MV, Rodahl M, Jonson M, Kasemo B. Viscoelastic acoustic response of layered polymer films at fluid-solid interfaces: continuum mechanics approach. *Physica Scripta.* 1999; 59:391–396.
46. Cleveland WS, Devlin ST. Locally weighted regression: An approach to regression analysis by local fitting. *J Am Stat Assoc.* 1988; 83:596–610.
47. Eisele NB, Andersson FI, Frey S, Richter RP. Viscoelasticity of thin biomolecular films: A case study on nucleoporin phenylalanine-glycine repeats grafted to a histidine-tag capturing QCM-D sensor. *Biomacromolec.* 2010; 13:2322–2332.
48. Vörös J, Ramsden JJ, Csúcs G, Szendro I, De Paul SM, Textor M, Spencer ND. Optical grating coupler biosensors. *Biomaterials.* 2002; 23:3699–3710. [PubMed: 12109695]
49. Tiefenthaler K, Lukosz W. Sensitivity of grating couplers as integrated-optical chemical sensors. *J Opt Soc Am B.* 1989; 6:209–220.
50. de Feijter JA, Benjamins J, Veer FA. Ellipsometry as a tool to study the adsorption of synthetic and biopolymers at the air-water interface. *Biopolymers.* 1978; 17:1759–1772.
51. Ball V, Ramsden JJ. Buffer dependence of refractive index increments of protein solutions. *Biopolymers.* 1998; 46:489–492.
52. Vörös J. The density and refractive index of adsorbing protein layers. *Biophys J.* 2004; 87:553–561. [PubMed: 15240488]
53. Sander M, Madlinger M, Schwarzenbach RP. Adsorption of transgenic insecticidal Cry1Ab protein on SiO₂. 1. Forces driving adsorption. *Environ Sci Technol.* 2010; 44:8870–8876. [PubMed: 21033745]
54. Hansma HG, Kim KJ, Laney DE, Garcia RA, Argaman M, Allen MJ, Parson SM. Properties of biomolecules measured from atomic force microscope images: A review. *J Struct Biol.* 1997; 119:99–108. [PubMed: 9245749]
55. Scheinthal BM, Bettelheim FA. Multiple forms of sialic acids. *Carbohydr Res.* 1968; 6:257–265.
56. Rudd PM, Endo T, Colominas C, Groth D, Wheeler SF, Harvey SF, Wormald MR, Serban H, Prusiner SB, Kobata A, Raymond DA. Glycosylation differences between the normal and pathogenic prion protein isoforms. *Proc Natl Acad Sci US A.* 1999; 96:13044–13049.
57. Stahl N, Baldwin MA, Teplow DB, Hood L, Gibson BW, Burlingame AL, Prusiner SB. Structural studies of the scrapie prion protein using mass spectrometry and amino acid sequencing. *Biochem.* 1993; 32:1991–2002. [PubMed: 8448158]
58. Bergström L. Hamaker constants of inorganic materials. *Adv Colloid Interfac.* 1997; 70:125–169.
59. Bhattacharjee S, Ko CH, Elimelech M. DLVO interaction between rough surfaces. *Langmuir.* 1998; 14:3365–3375.

60. Madliger M, Gasser CA, Schwarzenbach RP, Sander M. Adsorption of transgenic insecticidal Cry1Ab protein to silica particles. Effects on transport and bioactivity. *Environ Sci Technol*. 2011; 45:4377–4384. [PubMed: 21526821]
61. Saunders SE, Yuan Q, Bartz JC, Bartelt-Hunt S. Effects of solution chemistry and aging time on prion protein adsorption and replication of soil-bound prions. *PLoS ONE*. 2011; 6:e18752. [PubMed: 21526178]
62. Vasina EN, Déjardin P, Rezaei H, Grosclaude J, Quiquampoix H. Fate of prions of soil : Adsorption kinetics of recombinant unglycosylated ovine prion protein on mica in laminar flow conditions and subsequent desorption. *Biomacromolec*. 2005; 6:3425–3432.
63. Rigou P, Rezaei H, Grosclaude J, Staunton S, Quiquampoix H. Fate of prions in soil : Adsorption and extraction by electroelution of recombinant ovine prion protein from montmorillonite and natural soils. *Environ Sci Technol*. 2006; 40:1497–1503. [PubMed: 16568762]
64. Cooke CM, Shaw G. Fate of prions in soil: Longevity and migration of recPrP in soil columns. *Soil Biol Biochem*. 2007; 39:1181–1191.
65. Rao MA, Russo F, Granata V, Berisio R, Zagari A, Gianfreda L. Fate of prions in soil: Interaction of a recombinant ovine prion protein with synthetic humic-like complexes. *Soil Biol Biochem*. 2007; 39:493–504.
66. Wopfner F, Weidenhöfer G, Schneider R, von Brunn A, Gilch S, Schwarz TF, Wener T, Schätzl HM. Analysis of 27 mammalian and 9 avian PrPs reveals high conservation of flexible regions of the prion protein. *J Mol Biol*. 1999; 1163–1178. [PubMed: 10373359]
67. Hiemstra T, Yong H, Van Riemsdijk WH. Interfacial charging phenomena of aluminum (hydr)oxides. *Langmuir*. 1999; 15:5942–5955.
68. Appel C, Ma LQ, Rhue RD, Kennelley E. Point of zero charge determination in soils and minerals via traditional methods and detection of electroacoustic mobility. *Geoderma*. 2003; 113:77–93.
69. Brinza L, Benning LG, Statham PJ. Adsorption studies of Mo and V onto ferrihydrite. *Mineral Mag*. 2008; 72:385–388.
70. Nichols TA, Pulford B, Wyckoff AC, Meyerett C, Michel B, Gertig K, Hoover EA, Jewell JE, Telling GC, Zabel MD. Detection of protease-resistant cervid prion protein in water from a CWD-endemic area. *Prion*. 2009; 3:171–183. [PubMed: 19823039]
71. Tomaszewski JE, Madliger M, Pedersen JA, Schwarzenbach RP, Sander M. Adsorption of insecticidal Cry1Ab protein to humic substances. 2. Influence of humic and fulvic acid charge and polarity characteristics. *Environ Sci Technol*. 2012; 46:9932–9940. [PubMed: 22862550]
72. Ohshima H. Henry's function for electrophoresis of a cylindrical colloidal particle. *J Coll Interfac Sci*. 1996; 180:299–301.
73. Lemmon, EW.; McLinden, MO.; Friend, DG. Thermophysical Properties of Fluid Systems in NIST Chemistry WebBook. In: Linstrom, PJ.; Mallard, WG., editors. NIST Standard Reference Database Number 69. National Institute of Standards and Technology; Gaithersburg MD, 20899: <http://webbook.nist.gov> [accessed October 28, 2012]

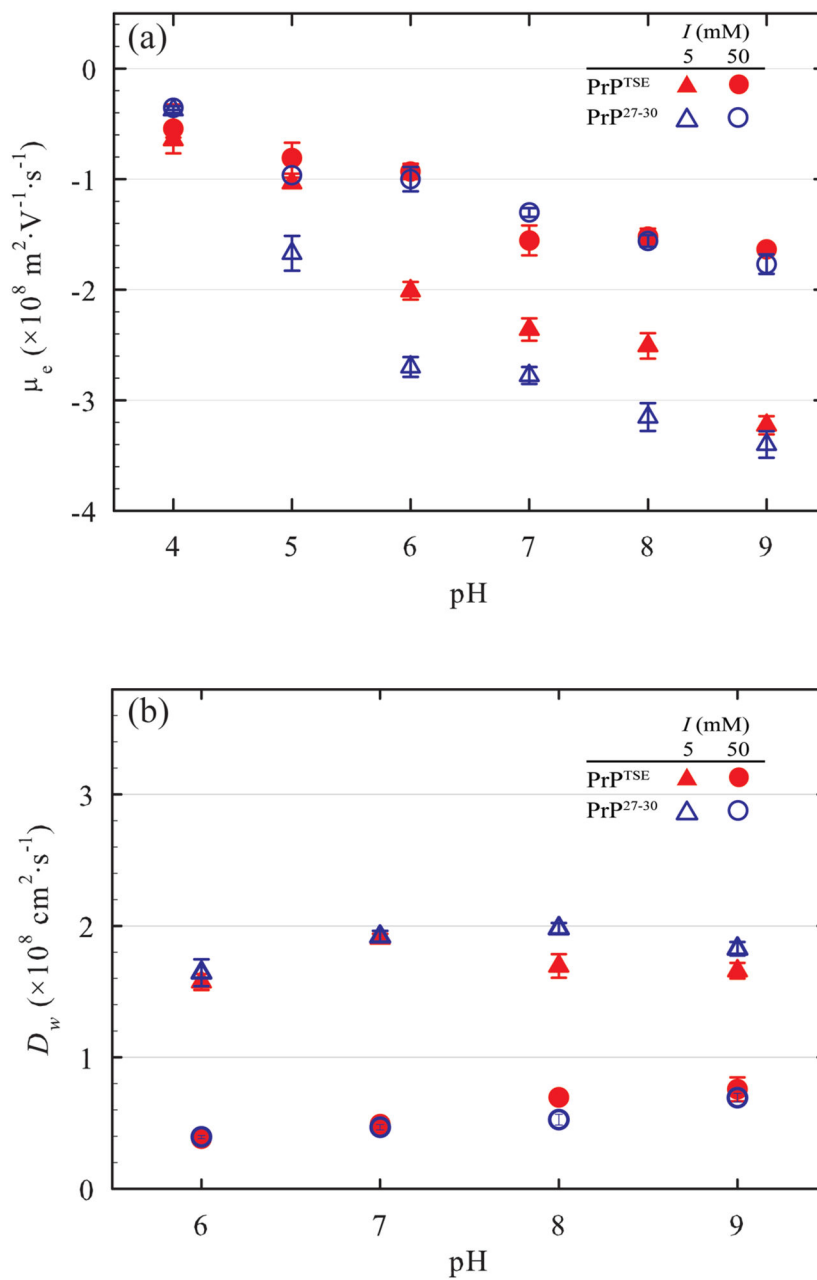


Figure 1. (a) Electrophoretic mobilities (μ_e) and (b) diffusivities in water (D_w) of the purified prion protein fibrils as a function of pH at ionic strengths of 5 and 50 mM. Despite the abundance of positively charged residues in PrP, the purified fibrils exhibit negative μ_e values at all tested pH values. As a point of reference, Figure S3 displays the μ_e data as apparent ζ -potentials estimated using a uniform cylinder assumption.⁷²

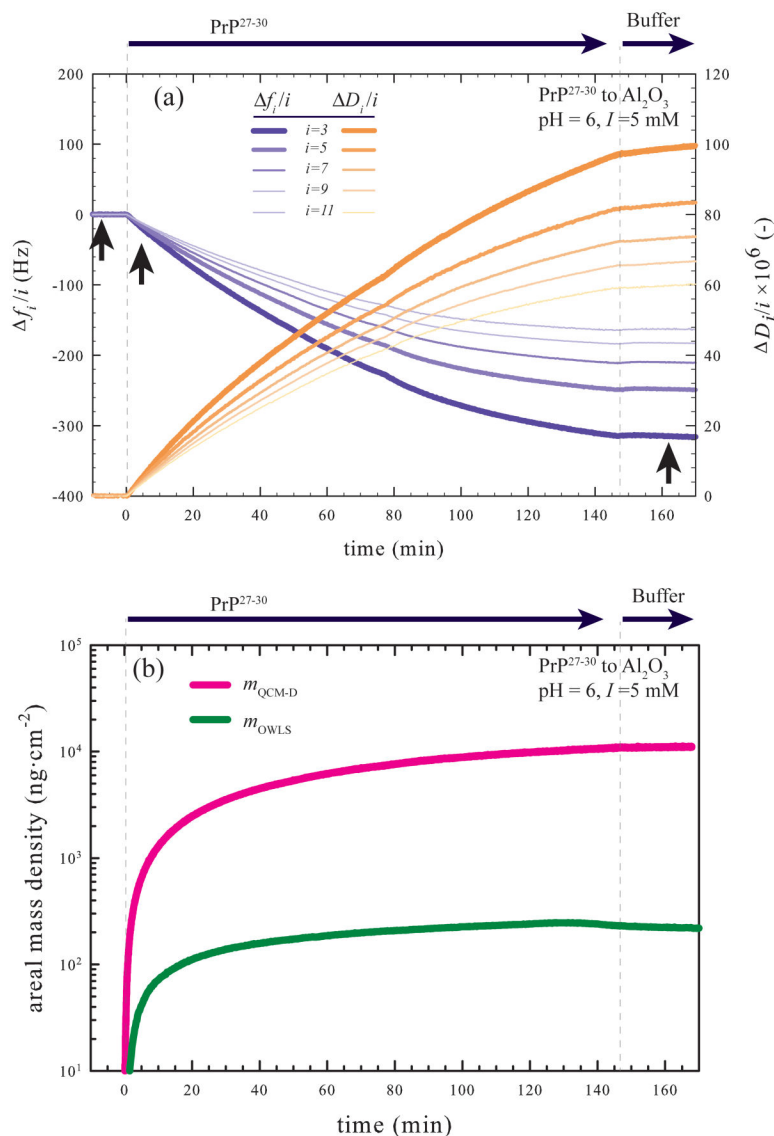


Figure 2.

(a) Representative QCM-D data recording PrP²⁷⁻³⁰ fibril attachment to Al₂O₃ at pH 6, $I = 5$ mM. Upward facing arrows indicate the time points that sensors were removed for AFM imaging (see Figure 4). (b) Areal mass densities of prion fibrils on Al₂O₃ as determined by QCM-D ($m_{\text{QCM-D}}$) and OWLS (m_{OWLS}). $m_{\text{QCM-D}}$ was determined by applying a Kelvin-Voigt viscoelastic model⁴⁵ to the f_i/i and D_i/i data. The density of the adlayer and the density and dynamic viscosity of the bulk phase were set at $1025 \text{ kg}\cdot\text{m}^{-3}$, $0.997 \text{ kg}\cdot\text{m}^{-3}$ and $0.000910 \text{ Pa}\cdot\text{s}$, respectively. $m_{\text{QCM-D}}$ includes the mass of all molecules acoustically coupled to the vibrating sensor surface including analyte and solvent (viz. PrP²⁷⁻³⁰ and water). m_{OWLS} was calculated by applying de Feijter's equation (eq 1) to the refractive indices measured by the instrument. The experimental effective refractive indices are measured relative to their initial (protein-free buffer) values, m_{OWLS} corresponds to the mass of only the analyte molecules (e.g., PrP²⁷⁻³⁰) not trapped solvent. Changes in solution chemistries are indicated by arrows above and dashed lines in each plot.

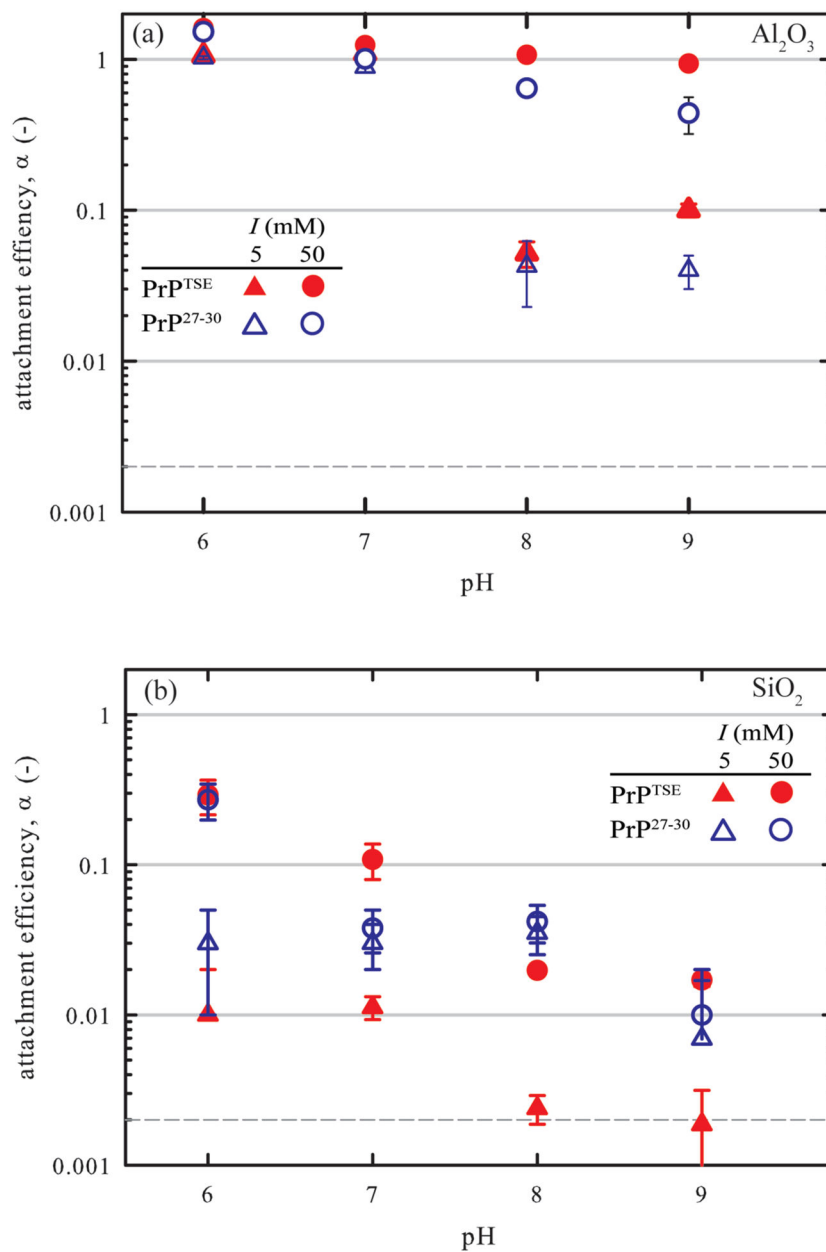


Figure 3. Attachment efficiencies (α) for PrP^{TSE} and PrP^{27-30} attachment to (a) Al_2O_3 and (b) SiO_2 as a function of pH at $I = 5$ mM and 50 mM. Error bars represent standard deviations of calculated attachment efficiencies of triplicate measurements. The horizontal dashed lines show the minimum detectable attachment efficiencies (SI).

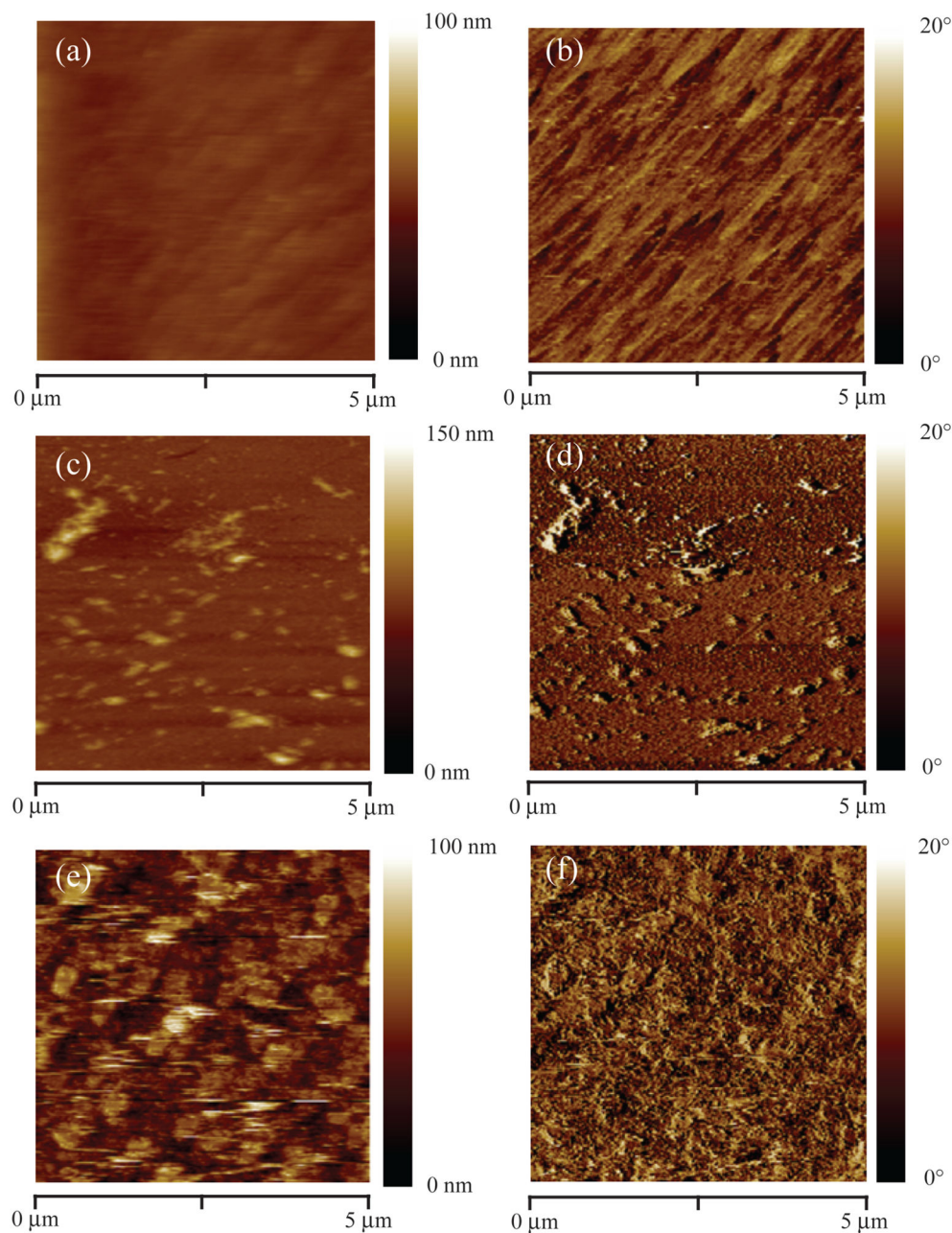


Figure 4. PrP²⁷⁻³⁰ adlayer formation on Al₂O₃ (pH 6, $I = 5\text{mM}$) imaged by AFM: (a) topographical and (b) phase images for the bare surface; (c) topographical and (d) phase images of the surface after 5 min of PrP²⁷⁻³⁰ attachment ($f_5/5 = -17\text{ Hz}$); and (e) topographical and (f) phase images of the fully developed adlayer (146 min of PrP attachment, $f_5/5 = -248\text{ Hz}$) Sampling times are indicated on Figure 2a. All sensors were rinsed with protein-free buffer prior to removal from the QCM-D and imaging.

Table 1

Final Areal Mass Densities and Properties for PrP²⁷⁻³⁰ Adlayers on Model Oxide Surfaces^a

Surface	pH	$f_{5, \max}^2$ (Hz)	d_{QCM-D} (nm)	m_{QCM-D} (ng-cm ⁻²)	m_{OWLS} (ng-cm ⁻²)	θ_w (%)	η_{final} (·10 ³ Pa·s ⁻¹)	G (MPa)
Al ₂ O ₃	6	-248 (1.7)	108 (1)	11080 (70)	212 (3)	98.1	2.6 (0.13)	0.145 (0.002)
	7	-144 (2.1)	57 (1)	5870 (40)	154 (6)	97.8	1.8 (0.08)	0.112 (0.001)
SiO ₂	6	-1.3 (0.1)	ND	ND	14.3 (0.9)	ND	ND	ND
	7	-0.9 (0.1)	ND	ND	12.1 (0.6)	ND	ND	ND

^a Kelvin-Voigt continuum viscoelastic modeling⁴⁵ was conducted to estimate m_{QCM-D} , η_a , and G using the measured bulk fluid density, $\rho_w = 997 \text{ kg}\cdot\text{m}^{-3}$, and the viscosity of water at 24.0 °C $\eta_w = 0.000910 \text{ Pa}\cdot\text{s}$.⁷³ were used as model inputs. An adlayer density, $\rho_a = 1025 \text{ kg}\cdot\text{m}^{-3}$ was iteratively selected to minimize differences between the recorded data and the model output. The adlayer water content was calculated as $\theta_w = 1 - (m_{OWLS}/m_{QCM-D})$. Abbreviations: d_{QCM-D} modeled adlayer thickness; G , complex shear modulus of adlayer; m_{QCM-D} , acoustic mass of adlayer; m_{OWLS} , optical mass of adlayer; ND, not determined; η_a , adlayer viscosity; θ_w , adlayer water content. Mean values are presented; error is one standard deviation.